



Article

Simulation and Design of an Underwater Lidar System Using Non-Coaxial Optics and Multiple Detection Channels

Yongqiang Chen ^{1,2}, Shouchuan Guo ^{1,3}, Yan He ^{1,2,4,*}, Yuan Luo ¹, Weibiao Chen ^{1,2,3,4}, Shanjiang Hu ¹, Yifan Huang ^{1,2}, Chunhe Hou ¹ and Sheng Su ¹

¹ Key Laboratory of Space Laser Communication and Detection Technology, Shanghai Institute of Optics and Fine Mechanics, Chinese Academy of Sciences, Shanghai 201800, China

² Center of Materials Science and Optoelectronics Engineering, University of Chinese Academy of Sciences, Beijing 100049, China

³ School of Physical Science and Technology, ShanghaiTech University, Shanghai 201210, China

⁴ Department of Guanlan Ocean Science Satellites, Pilot National Laboratory for Marine Science and Technology, Qingdao 266237, China

* Correspondence: heyans@siom.ac.cn

Abstract: The efficacy of underwater laser detection is considerably impacted by the intense attenuation of light resulting from the scattering and absorption effects of water. In this study, we present the simulation and design of the underwater Lidar system that integrates the paraxial multi-channel detection strategy to enhance the dynamic range in subsea environments. To evaluate the performance of the system with multiple detection channels, we introduce a multi-channel underwater Lidar simulation (MULS) method based on the radiative transfer Lidar equations. Experimental validations were conducted under varied water conditions to assess the performance of the prototype and validate the simulation results. The measured range accuracy of each channel in the prototype is better than 0.1085 m, and the simulated and measured waveforms exhibit strong correlations, verifying the reliability and validity of the simulation method. The effects of transceiver configuration and the maximum detectable range of different detection methods were also discussed. Preliminary results indicate that the paraxial multi-channel design effectively suppresses near-field backscattering and substantially enhances the maximum detectable range. The findings presented in this study may provide valuable insights for the design and optimization of future underwater laser detection systems.

Keywords: underwater; simulation; non-coaxial; multi-channel; Lidar



Citation: Chen, Y.; Guo, S.; He, Y.; Luo, Y.; Chen, W.; Hu, S.; Huang, Y.; Hou, C.; Su, S. Simulation and Design of an Underwater Lidar System Using Non-Coaxial Optics and Multiple Detection Channels. *Remote Sens.* **2023**, *15*, 3618. <https://doi.org/10.3390/rs15143618>

Academic Editors: Teodosio Lacava, Atul Kumar Srivastava, Panuganti C.S. Devara and Vijay K. Soni

Received: 25 May 2023
Revised: 17 July 2023
Accepted: 18 July 2023
Published: 20 July 2023



Copyright: © 2023 by the authors. Licensee MDPI, Basel, Switzerland. This article is an open access article distributed under the terms and conditions of the Creative Commons Attribution (CC BY) license (<https://creativecommons.org/licenses/by/4.0/>).

1. Introduction

In recent years, there has been growing recognition of the scientific significance, economic benefits, and strategic importance of ocean surveys, which has contributed to the accelerated development of technologies, such as underwater sensor networks [1] and underwater vehicles [2]. Therefore, there is an increasing demand for advanced underwater detection technology to support marine survey activities. Light Detection and Ranging (Lidar), as a widely used active remote sensing technique, has been extensively used in various fields, including topographic mapping [3], bathymetry [4], atmospheric remote sensing [5], forest management [6], and underwater target detection [7].

Initially, laser-based underwater target detection focused on mapping seabed depth and topography using airborne Lidar systems [8,9]. With the maturity of high-power miniaturized pulsed lasers and the growing development of high-sensitivity detectors, underwater Lidar has gradually become a powerful tool for subsea exploration. Currently, a few high-quality systems have found applications in offshore ocean exploration [10], marine habitat surveys [11], underwater mine detection [12], and seabed cable surveys [13].

However, underwater laser detection faces challenges due to the strong attenuation of light caused by the scattering and absorption effects of water. These limitations affect the performance of underwater Lidar systems, restricting their maximal detectable range and accuracy. Consequently, scientists have investigated various techniques to improve the performance of underwater detection, such as selecting an optimal laser source [14], photon counting [15], polarization detection [2], and range-gating [16], etc. Among these technologies, the range-gated approach has become a primary means of achieving long-range target detection in the underwater environment, which filtered out near-field backscattering by adjusting the delay between the detector's gate open time and the emitted laser pulse. Unfortunately, this method requires prior knowledge of the target distance and has a blind zone, resulting in the limited detection dynamic range, which may not match the wide effective dynamic range requirement of underwater detection [17].

The intricacy and large dynamic range of target echoes, due to rapid attenuation of light in water, poses challenges for Lidar receivers. For example, a 10^5 dynamic range requires a high-speed digitizer with 16.6 bits, which is prohibitively expensive and unfeasible for the manufacture of Lidar. Research groups have developed signal dynamic-range compression techniques [18,19] that allow Lidar systems to achieve sufficient penetration depth with the use of low-cost digitizers featuring lower bits. Mitsubishi Electric Corporation [20], for instance, has devised a sensitivity time control (STC) circuit to minimize the undesirable backscattering signals. However, this method requires intricate design of gain curves dependent on the turbidity of measurement environment and might be sensitive to noise, resulting to variations in measured data. Other techniques [21,22], such as logarithmic amplification are unable to meet the high-frequency requirement for most profiling applications [17]. To overcome these issues, we propose a novel paraxial multi-channel underwater detection strategy that incorporates optical energy splitting, gated techniques, and high-low-gain settings. This approach can successfully broaden the dynamic range and suppress backscattering, without requiring sophisticated hardware circuit designs.

In the early design stage of Lidar systems, simulation approaches offer an effective way to interpret laser-medium interactions in Lidar signals and evaluate system performance without physically assembling the unit, which can save precious resources and time [23]. A wide range of Lidar simulators [24–31] have been developed based on the radiative transfer equation and the statistical Monte Carlo (MC) model, enabling comprehensive analysis and optimization of Lidar systems.

In 2012, Abdallah [24] et al. established the Wa-LiD simulator based on the underwater radiative transfer Lidar equation. This simulator considers the entire process of laser bathymetric transmission, integrates noise due to solar background and detector, and is suitable for simulating airborne or satellite Lidar waveforms [32]. In 2016, Kim and Kopilevich [26] developed a Lidar waveform simulator based on the small angle approximation (SAA) of radiation transfer equation (RTE) and reciprocity theorem, which predicts the general performance of bathymetric Lidar. In 2020, a spaceborne oceanic Lidar simulator based on the semi-analytic MC approach was built to analyze the detection performance [28]. More recently, an open-source SOLS simulator [29], which considers the Lidar system and environmental parameters, was developed to explore the detection potential capability of spaceborne oceanic Lidar [33]. Although various simulators have been developed for airborne or spaceborne oceanic Lidar, they are not designed for underwater applications and do not consider the transceiver geometry and detection channel configuration of Lidar systems in specific conditions.

In this study, we described both a method for simulating underwater Lidar measurements using a non-coaxial multi-channel sensor and the design of a prototype instrument. The proposed multi-channel underwater Lidar simulation (MULS) method is built upon equations derived from traditional hydrographic Lidar. It takes into account the Lidar overlap factor, the multi-channel detection settings, and the noise due to the data acquisition procedure. By incorporating these considerations, the MULS method enables the simultane-

ous waveform simulation of multiple channels, providing a comprehensive understanding of the system's performance.

To validate the effectiveness of the proposed paraxial multi-channel detection strategy in suppressing near-field backscattering and enhancing the maximum detectable range of the Lidar system, we have designed an underwater Lidar prototype utilizing non-coaxial optics and multiple detection channels. This prototype incorporates separate receivers for the near-field (two channels) and the far-field, with only the latter being range-gated. Experimental validations were conducted under diverse water conditions to evaluate the performance of the prototype and validate the simulation results. The results of the experiment and simulation in different scenarios are well-matched, which proves the effectiveness and necessity of the optimization.

The rest of the paper is organized as follows: In Section 2, we present the fundamental basis of underwater Lidar detection, the simulation model, and the flowchart of the MULS method. Section 3 provides a brief description of the designed underwater Lidar system. The range performance of the system and the comparison between simulation and experimental data are shown in Section 4. In Section 5, we further explore the impacts of transceiver configuration on the signal strength and estimate the maximum detectable range under various seawater conditions. A conclusion of this work along with an outlook of future application are outlined in the last section.

2. Principle and Methods

2.1. Principle of the Underwater Lidar

The basic principle underlying underwater Lidar detection is represented in Figure 1. Laser pulses are transported via the optical window, the water column, and towards an underwater target. Then, the back-reflected energy is captured by the receiver and transformed to the electrical signal. The echo signal of the underwater Lidar includes the signal reflected by the optical window, backscattered signal from the water column, target-reflected signal and background light noise. Thus, the echo signal intensity function can be mathematically defined as the sum of the echo intensity backscattered from the consecutive media encountered by the emitted laser beam, and background light source [24].

$$P_T(t) = P_S * w(t_s) + P_C * w(t_c) + P_U * w(t_u) + P_{bg} \quad (1)$$

where $P_T(t)$ is the total power, t is the time scale; P_S , P_C , P_U , and P_{bg} are the received power from optical window, water column, underwater target and background light, respectively; and $w(t_x)$ is the heavy-tailed distribution [34] of the emitted laser pulse, as follows:

$$w(t_x) = \left[\frac{k(t - t_x)}{\Delta t} \right]^n \exp \left[\frac{-k(t - t_x)}{\Delta t} \right] \quad (2)$$

where t_x is the two-way time delay of the emitted laser pulse between the laser and the optical window t_s , water column t_c or underwater target t_u ; Δt is the laser pulse width; k is a constant related to Δt ; and n indicates the laser pulse's temporal shape [35], usually $n = 1$.

The presence of strong internally reflected light occurs when the laser beam passes through the optical window into the water. The power P_S returned from the optical window can be described by the laser-radar equation [24], which is traditionally applicable mainly in the far-field region. However, in our specific non-coaxial design, we inherently consider the near-field conditions to a certain extent. This is indicated by Lidar overlap factor O , which is determined by the Lidar geometric configuration and approaches zero in the near-field region. The equation representing the power P_S is as follows [36]:

$$P_S = P_t \cdot A_r \cdot O \cdot \frac{\eta_t \eta_o T_s}{D^2} \quad (3)$$

where $P_t = E_t / \Delta t$ is the peak power of the laser pulse, E_t is the emitted single pulse laser energy, T_s is the Fresnel reflectance at the optical window, and η_t and η_o are the optical

efficiency of the transmitter and receiver system. For the calculation of power from the optical window in our study, the overlap factor equal to zero due to very close distance to the optical window, A_r is the receiver area, and D is the distance between the receiver and optical window.

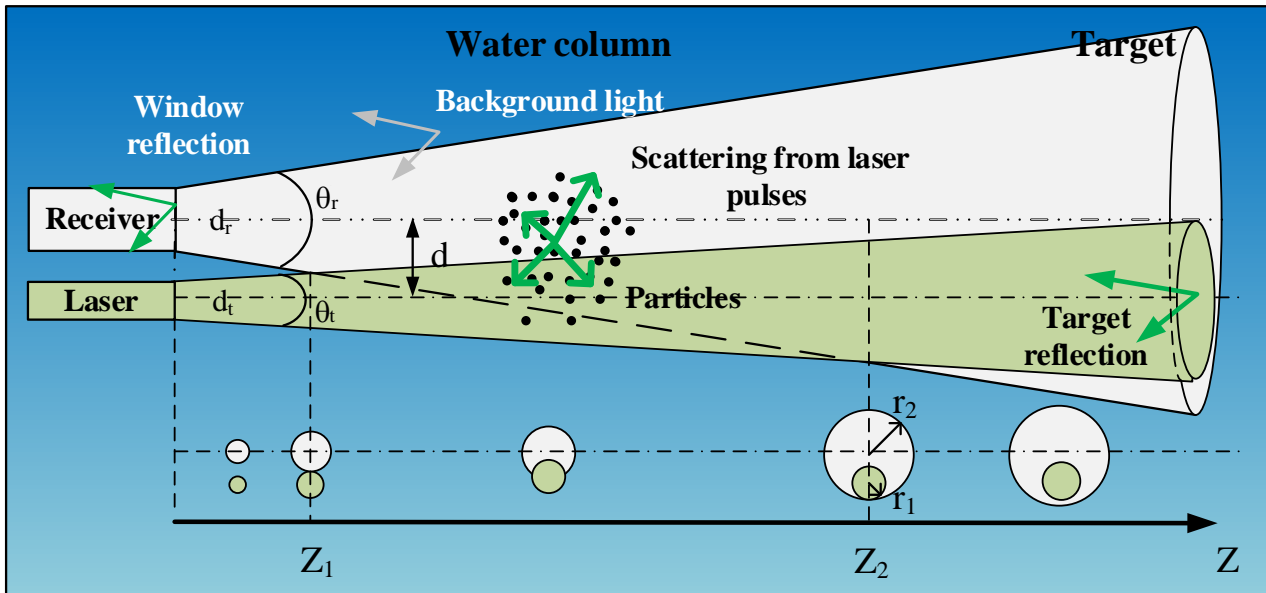


Figure 1. The basic principle of the underwater laser detection.

The signal returned from the water column [29,37] is described as follows:

$$P_c(z) = P_t \cdot A_r \cdot O(z) \cdot \beta_\pi \frac{\eta_t \eta_o (1 - T_s)^2}{z^2} \cdot \exp(-2k_{lidar} \cdot z) \tag{4}$$

where z is the depth of water column, and β_π is the volume scattering coefficient at a scattering angle of π radians, which can be expressed as:

$$\beta_\pi = b \cdot \frac{\tilde{\beta}_{HG}(g, \pi)}{2\pi \int_{\pi/2}^{\pi} \tilde{\beta}(g, \theta) \sin(\theta) d\theta} \tag{5}$$

where b is the total scattering coefficient, θ is the scattering angle, $\tilde{\beta}_{HG}$ represents the Henyey–Greenstein scattering phase function [38], and $g = 0.924$ is the asymmetry parameter.

The parameter k_{Lidar} is the Lidar attenuation coefficient that is given by [39]:

$$k_{lidar} = c[0.19(1 - w_0)]^{\frac{w_0}{2}} \tag{6}$$

where c is the attenuation coefficient that can be expressed as the sum of the scattering coefficient b , and absorption coefficient a , $c = a + b$, $w_0 = b/c$ is the single scattering albedo.

The received power from the underwater target [20,40] is written by:

$$P_U = P_t \cdot A_r \cdot O(Z) \cdot \frac{\rho_b}{\pi} \frac{\eta_t \eta_o (1 - T_s)^2}{Z^2} \cdot \exp(-2k_{lidar} \cdot Z) \tag{7}$$

where Z is the distance of measured target, and ρ_b is the reflectance of the target.

In the underwater environment, ambient light sources comprise solar radiation and artificial light. Solar light undergoes cumulative diffusion and exponential attenuation as it permeates seawater. However, in deep water environments where sunlight cannot penetrate, the solar radiation level becomes insignificant. In this case, artificial light sources

become the main source of background light. The expression of the received background light power is given by:

$$P_{bg} = P_{bgTar} + P_{bgSca} \quad (8)$$

$$P_{bgTar} = L_b \cdot A_r \cdot \eta_o \cdot \rho_b \cdot \frac{\theta_r^2}{4} \cdot \Delta\lambda \cdot \exp(-2k_{lidar} \cdot Z) \quad (9)$$

$$P_{bgSca} = L_b \cdot A_r \cdot \eta_o \cdot \beta_\pi \cdot \frac{\pi\theta_r^2}{4} \cdot \Delta\lambda \cdot \exp(-2k_{lidar} \cdot Z) \quad (10)$$

where P_{bgTar} is the background power that is reflected from the target; P_{bgSca} is the background power scattered off of particles; θ_r is the field of view of the receiver; $\Delta\lambda$ is the bandwidth of the optical filter; and L_b is the spectral radiance of background light, which is generate by modeling the artificial light source.

2.2. Simulation Model

The proposed MULS method is based on equations from traditional hydrographic Lidar models and takes into account both the Lidar geometrical representation of the transceiver configuration and the multi-channel photovoltaic detection process. This approach also considers the superposed noise of detector noise and quantization noise during the data acquisition procedure. Figure 2 depicts the flow chart of the MULS method. The simulation begins with the initialization of simulation parameters, such as Lidar geometry parameters, system parameters, environmental parameters, and detection parameters. Then, the optical signal level (P_S , P_C , P_U , and P_{bg}) and total optical signal P_T are calculated based on Equations (1)–(10). Next, the total optical signal is divided into a far-field signal and near-field signal by the beam splitter with a particular ratio and converted into electrical signals. Multiple channels with different gains can be obtained by splitting the output electrical signal from the detector. Lastly, the simulated multi-channel output waveforms corresponding to intensity as a function of time t are generated. The details of the simulation model are described in the following sections.

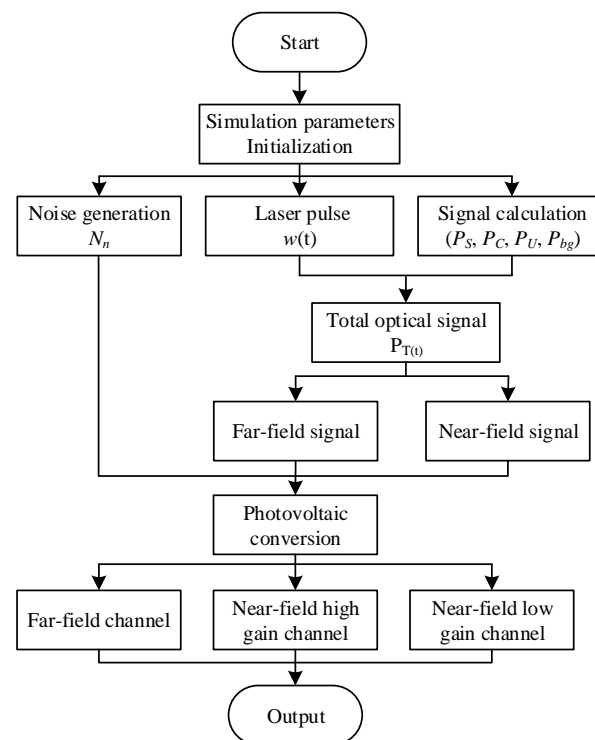


Figure 2. Flow chart of the MULS method.

2.2.1. Lidar Geometric Model

The geometric configuration of a Lidar transceiver has a significant impact on the echo signal intensity, which can be quantified by the overlap factor in the laser-radar equation. In this study, we adapt a non-coaxial structure with independent transmitting and receiving optical paths. Additionally, the emitting laser beam is always parallel to the optical path of the receiver.

Figure 1 depicts the typical structure of a non-coaxial underwater Lidar system. The geometric offset between the laser and the receiver is d , d_t is the spot diameter of laser beam, θ_t is the divergence angle, the diameter of the receiver is d_r , and the field of view is θ_r . Assuming that the detection and laser-illuminated regions are circular, the radius of the illuminated area is denoted as r_1 , and the radius of the detection area is r_2 . As the target distance Z increases, the laser-illuminated region and detection area begin to overlap, and the overlap area is designated as the effective detection area. The Lidar overlap factor $O(Z)$, which is a function of the distance Z , can be written as the effective detection area divided by the laser-illuminated area A_t , and is given by:

$$O(Z) = \begin{cases} 0 & Z \leq Z_1 \\ \frac{(\omega_1 - \sin\omega_1)r_1^2 + (\omega_2 - \sin\omega_2)r_2^2}{2\pi r_1^2} & Z_1 < Z < Z_2 \\ 1 & Z \geq Z_2 \end{cases} \quad (11)$$

where ω_1 and ω_2 is the overlapping sector angle corresponding to the laser-illuminated area and detection area, and can be calculated by the law of cosines. If the distance Z is lower than Z_1 , the Lidar has a detection blind area, and the overlap factor $O(Z)$ is equal to zero. Conversely, when the distance Z is higher than Z_2 , the laser-illuminated area and detection area of the system start to coincide with an overlap factor close to one. Additionally, for Lidar systems with a coaxial structure, the overlap factor is usually equal to one.

2.2.2. Multiple Channels Detection Model

The received optical signal is converted into electrical signal by the detector and then transformed into a digitized value by the analog-to-digital converter (ADC). Due to the wide dynamic range of the echo signal in the underwater environment, a multi-channel signal detection strategy is adopted. The optical signal is separated into a near-field signal and a far-field signal by a beam splitter. The near-field channel is further split into a high-gain channel and a low-gain channel by dividing the electrical signal output from the detector in a specified proportion. Based on the multiple channels detection characteristics of the system, a detection model is established.

The output voltage signal of the detectors is given by:

$$V_i(t) = \xi_i \cdot \xi_v \cdot S_k \cdot M \cdot P_T(t) \cdot R_L \quad (12)$$

where ξ_i is the beam splitting ratio of the detection channel, ξ_v is the output voltage ratio, S_k is the detector sensitivity, M is gain of the detector, P_T is the optical signal power, and R_L is the feedback resistor (50 Ω).

The voltage signal V_i is sampled and converted to digitized value by the data acquisition unit. For our multi-channel underwater Lidar system, the relationship between the voltage signal V_i and the digitized Lidar sampled signal U_i can be expressed as [41]:

$$U_i(t) = \frac{V_i(t)}{V_d} \cdot 2^{Bit} + N_n(t) \quad (13)$$

where V_d is the reference voltage level, Bit is the resolution of the ADC, and $N_n \sim N(\mu, \sigma_n^2)$ is detection noise which can be approximated by the Gaussian distribution [42]. The mean value μ and the variance σ_n of the noise are measured by experiments.

3. Description of Underwater Lidar System

Figure 3 depicts the schematic diagram of the multi-channel underwater Lidar (MUL) system. The system comprises a laser transmitter subsystem, a signal receiver subsystem, a scanner, a system controller, and a data acquisition unit. The primary parameters of the MUL system are listed in Table 1. The transmitter is a 532 nm pulsed laser with a repetition rate of 5 kHz, with a single pulse energy of over 500 μ J, and a pulse width of approximately 10 ns. Three 45-degree reflecting mirrors (RM1, RM2, and RM3) reflect the majority of the emitted laser pulse energy, which is then used to illuminate the underwater target, while a PIN photodiode detects the remaining laser pulse energy as the reference signal (CH0).

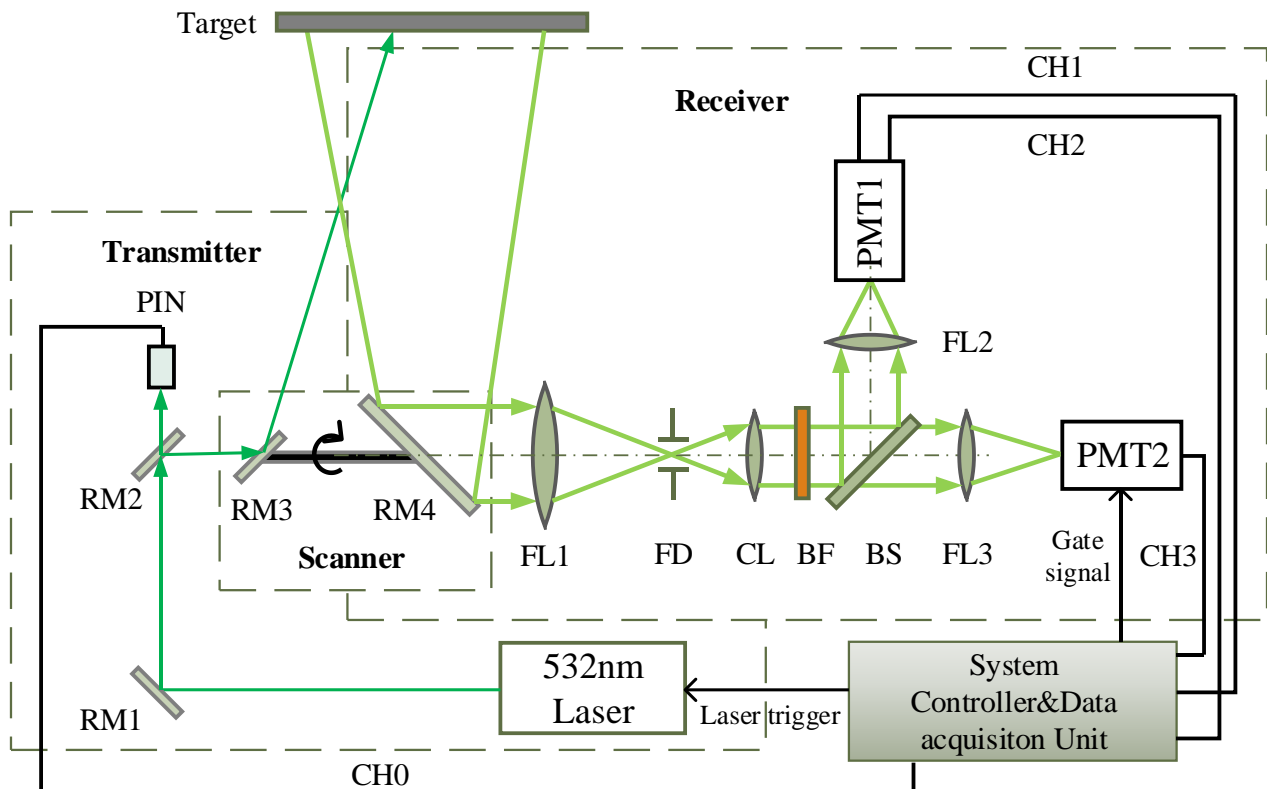


Figure 3. Schematic diagram of the underwater Lidar system. RM1, RM2, RM3, RM4, reflecting mirror1, 2, 3, 4; FL1, FL2, FL3, focusing lens1, 2, 3; FD, field diaphragm; CL, collimating lens; BF band-pass filter; BS, beam splitter; PIN, photon diode; PMT1, PMT2, photomultiplier tube1, 2; CH0, CH1, CH2, CH3, CH4, channel 0, 1, 2, 3.

The system employs a non-coaxial transceiver design, hence the transmitter and receiver channels do not share the same optical path. This configuration effectively decreases the effects of internally reflected light from the emitting optical components and suppress the backscattering of the near-field water column. The scanner drives the transmitter mirror (RM3) and the reception mirror (RM4) to revolve on a common shaft, synchronously scanning a collimated laser beam and a limited field of view (FOV). By minimizing the shared volume between the transmitter and receiver, both forward scatter and backscatter effects are minimized utilizing synchronous scanning techniques.

Table 1. Primary parameters of the MUL system.

Transmitter	Wavelength λ	532 nm
	Pulse energy E_t	500 μ J
	Pulse width Δt	10 ns
	Laser repetition rate	5 kHz
	Beam divergence θ_t	2 mrad
	Beam diameter d_t	10 mm
Receiver	Receiver area A_r	$4.4 \times 10^{-3} \text{ m}^2$
	Geometric offset d	130 mm
	Field of view θ_r	50 mrad
	Filter bandwidth $\Delta\lambda$	1 nm @532 nm
	Optical efficiency η_o	60%
	Beam splitter ratio ξ_i	2:98
	Output signal ratio ξ_v	1:9
Detector	PMT1/PMT2	Non-gated/Gated mode
	Detector sensitivity S_{k1}/S_{k2}	77/77 mA/W
	Max. average anode current	100/100 μ A
	Effective area	$\varnothing 8/\varnothing 8 \text{ mm}$
Analog Digital Converter	Bandwidth	200 MHz
	Sampling rate	1 GS/s
	Resolution Bit	10 bits
	Channels	4
Others	Dimensions	$\varnothing 260 \text{ mm} \times 650 \text{ mm}$
	Weight	30 kg
	Supply voltage	380 V

The receiver subsystem of this system comprises three focusing lenses (FL1, FL2, and FL3), a collimating lens (CL), a field diaphragm (FD), a band-pass filter (BF), a beam splitter (BS), and two photomultiplier tubes (PMT1 and PMT2). The back-scattered light from the target and water column is focused by a primary lens (FL1) with a diameter of 75 mm and then collimated by lens CL. A field diaphragm at the focus of lens FL1 limits the system's field of view (FOV) to 50 milliradians. The narrow FOV, combined with the use of a narrow bandwidth filter, decreases the amount of background light collected by the receiver. The collimated light travels through a 1 nm band-pass filter (BF) and then a 2:98 ratio beam splitter (BS) divides the filtered light into two portions. The lower-energy portion of the laser beam is focused by lens FL2 and detected by the non-gated mode photomultiplier tube PMT1 (Hamamatsu H10720-01), with a radiant sensitivity of 77 mA/W and an effective area diameter of $\varnothing 8 \text{ mm}$. The output signal of PMT1 is further separated into the high-gain channel (CH1) and low-gain channel (CH2) with an output signal ratio of 9:1. The higher-energy portion of the laser beam is focused by lens FL3 and detected by a PMT detector PMT2 (Hamamatsu H11526-01), which has the same parameters as PMT1, except for the gated operation. This detector employed a gate circuit that activated the detection of the incident optical signal only when the gate signal was on. This mechanism allowed us to selectively capture the desired portion of the waveform by controlling the gate-open timing. This channel (CH3) is typically used for far-field signal detection utilizing the range-gated approach, which can suppress the near-field backscattering signals and only detects the target reflected signal. Then the output voltage signals of the detectors are captured by the data acquisition unit. This unit features four-channel analog-to-digital converters with an effective dynamic range of 10 bits and a sampling rate of 1 GS/s.

The system controller triggers the 532 nm laser to emit laser pulses at a frequency of 5 kHz. A gating signal with the same repetition rate is then applied to activate the PMT2, enabling it to detect the incident light. Users can alter the gate width and delay time of the gating signal by sending commands to the system controller. The system controller also implements the synchronized acquisition of experiment data from all four channels. Figure 4 presents the prototype of the MUL system and the corresponding timing sequence

diagram. The LiDAR system has a waterproof housing made of aluminum alloy, providing high-pressure resistance for underwater operation at depths of up to 100 m. The overall size of the prototype is 260 mm in diameter and 650 mm in length, with a weight of roughly 30 kg.

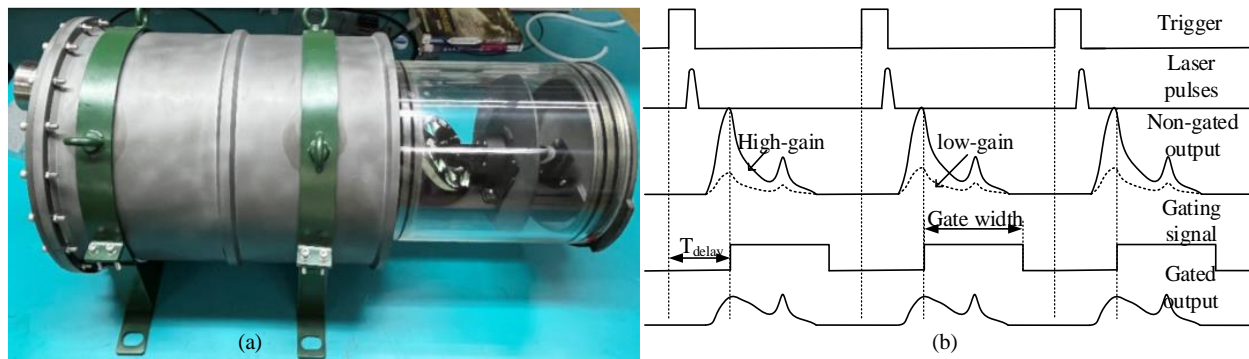


Figure 4. (a) Photograph of the prototype; (b) timing sequence diagram of the multi-channel system.

4. Simulation and Experimental Results

4.1. Detection Noise Analysis

The detection noise in the Lidar system is the combination noise of detector noise, amplifying circuit noise, and quantization noise. Figure 5a–c illustrate the superposed detection noise measured by the three detection channels (CH1, CH2, and CH3) in dark surroundings. The distribution of the noise measured by each channel is presented in Figure 5d–f, as well as the observed noise obeys the Gaussian distribution. It should be noted that each channel exhibits a distinct noise bias, which does not influence the overall noise distribution and can be corrected during the data processing procedure.

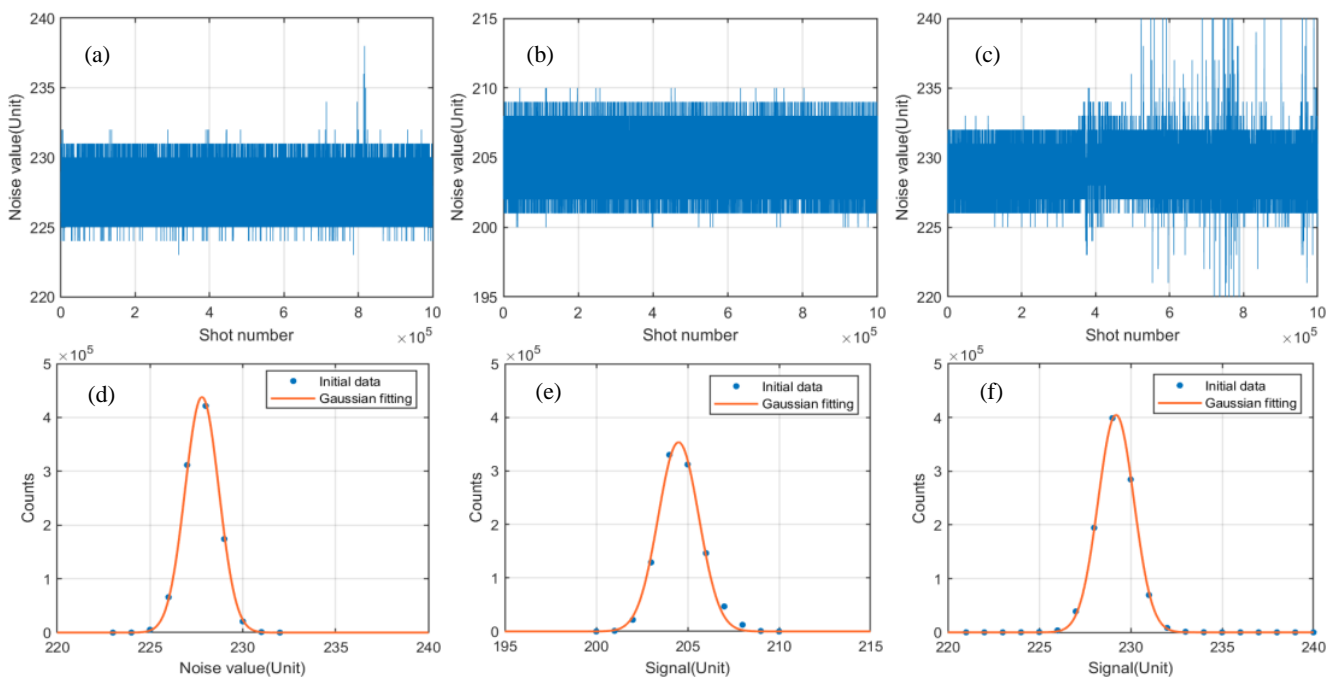


Figure 5. (a–c) The superposed detection noise of three detection channels: (a) CH1, (b) CH2, and (c) CH3 measured in the dark environments. (d–f) Respective distribution and Gaussian fitting of the noise measured by the three channels.

However, measuring the Poisson distributed shot noise is challenging due to its association with optical signals. According to the central limit theorem, the Poisson distribution can be approximated as a Gaussian distribution, when the number of incident photons within the signal is large [43]. Therefore, a Gaussian distribution model is employed to represent the shot noise [5]. The variance of shot noise, as described by Ehret et al. [44], is used to generate the simulated noise signals.

4.2. Anechoic Pond Verification Experiment

To assess the range accuracy of the system and to verify the reliability of the proposed simulation method, underwater detection experiments were undertaken on 1 December 2022. The experimental site was an anechoic pond at the Shanghai Acoustics Laboratory, Academia Sinica (ACS). The in situ water body parameters were collected by the WETLabs acs instrument, which recorded an attenuation coefficient (c) of 1.44 m^{-1} and an absorption coefficient (a) of 0.22 m^{-1} at 532 nm. The prototype and the target were submerged in the water and positioned on both sides of the pond. The target was a black-painted rectangular aluminum plate with a reflectance of 0.1. The distances between the prototype and the panel were adjusted at 8.5 m, 10.0 m, and 11.5 m accordingly. Figure 6 displays the photographs of the experimental scenario and the target.

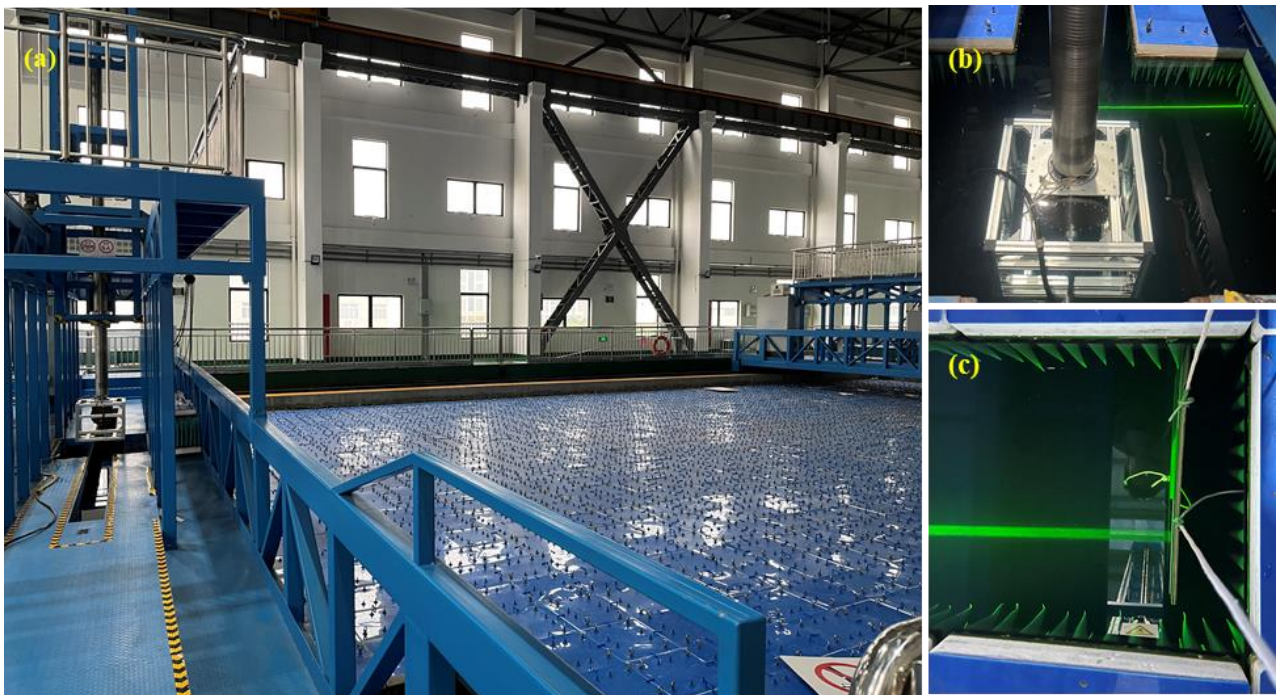


Figure 6. Verification experiments under anechoic pond environment. (a) The anechoic pond. (b) The mounted Lidar prototype. (c) The panel target.

The measured four-channel Lidar waveforms and peak detection results are displayed in Figure 7a–c. Channel 0 serves as the reference signal for monitoring the emitted laser pulses, channel 1 is the near-field high-gain channel, channel 2 is the near-field low-gain channel, and channel 3 is the far-field gated channel. The time interval value between the peak of reference channel 0 and the target peaks in channels (1–3) is determined by utilizing the peak detection methods [45]. The corresponding range value R_i of different detection channels can be represented as follows according to the TOF principle:

$$R_i = \frac{c_w \cdot t_i}{2} + \Delta R_i \quad (14)$$

where c_w is the speed of light in water, t_i is the time interval between the peak of reference channel 0 and the target peaks of the channel (1–3), and ΔR_i is the range offset constant measured through range calibration.

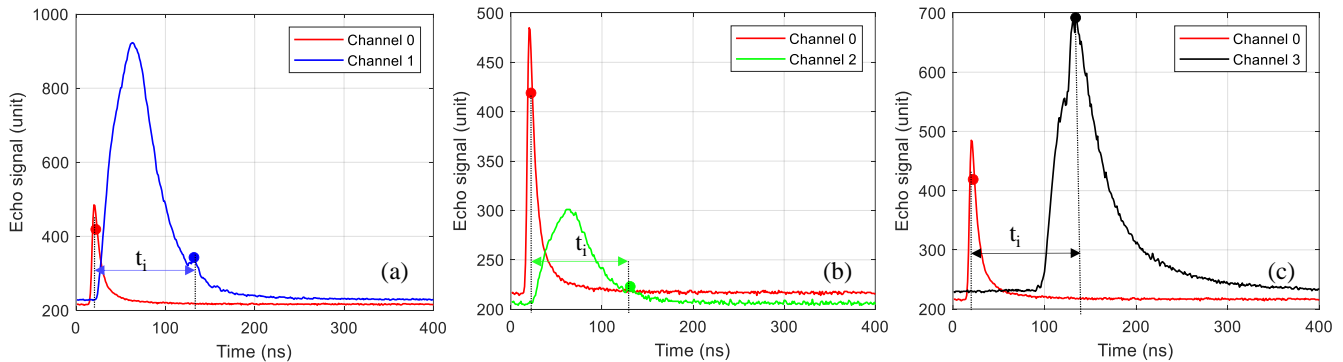


Figure 7. The four-channel Lidar waveform of the experiment and the peak detection results. (a) CH1: the near-field high-gain channel. (b) CH2: the near-field low-gain channel. (c) CH3: the far-field gated channel.

During the anechoic pond verification experiment, the Lidar operated in static mode, conducting one thousand measurements for the target at each position. The multi-channel measured distance data were analyzed to evaluate the ranging accuracy, taking into consideration both range precision and mean deviation [40]. The results of the range accuracy for channels 1–3 are presented in Table 2. The accuracy of all the detection channels decreases as the distance of the targets rises. The decline in accuracy is due to the reduction in the signal-to-noise ratio of the echo signal as the increase in target distance. Since the signal-to-noise ratio of channel 1 is larger than that of channel 2, the range accuracy of channel 1 is always better than that of channel 2. The results of the anechoic pond experiment reveal that the range accuracy of each detection channel is better than 0.11 m.

Table 2. The ranging accuracy of CH1, CH2, and CH3 in the anechoic pond.

Target Distance /m	Range Precision/m			Mean Deviation/m		
	CH1	CH2	CH3	CH1	CH2	CH3
8.5	0.0473	0.0664	0.0369	0.0417	0.053	0.0279
10.0	0.0674	0.0879	0.0447	0.0557	0.0736	0.0332
11.5	0.0896	0.1085	0.0733	0.0732	0.0931	0.0577

The proposed MULS approach was validated by comparing the simulated three-channel waveforms with the experimental results obtained from the anechoic pond. The simulated waveforms were generated using the systematic parameters specified in Table 1, the gain parameters (M1 and M2) for PMT1 and PMT2 (2000 and 20,000, respectively) and water column parameters of the pond. Figure 8a illustrates the simulated waveforms and the measured Lidar signals from the two near-field channels. The black dotted rectangular region represents the backscattering signal of the water column, while the red one represents the echo signal of a target located at a distance of 11.5 m. The strength of both the simulated and measured water column signal first grows and then decreases considering the influence of overlap factor and water attenuation. Despite the non-coaxial transceiver design, the strength of the near-field backscattering signal remains much higher than the target echo, leading some of the signal reflected from the target to be drowned in the invalid scattering signal. As shown in Figure 8a, the experimentally measured scattering signal from the water column exhibits a higher intensity than the simulated waveform in the near-field region (0–50 ns). This disparity can be attributed to the effects of multiple scattering,

which are more pronounced in this region. However, in the far-field region (50–350 ns), the impact of multiple scattering on signal intensity is negligible. Both the simulated and measured signals are well matched in this region. The comparison result indicates remarkable consistence between the simulated and measured waveforms, which verifies the accuracy of the MULS approach.

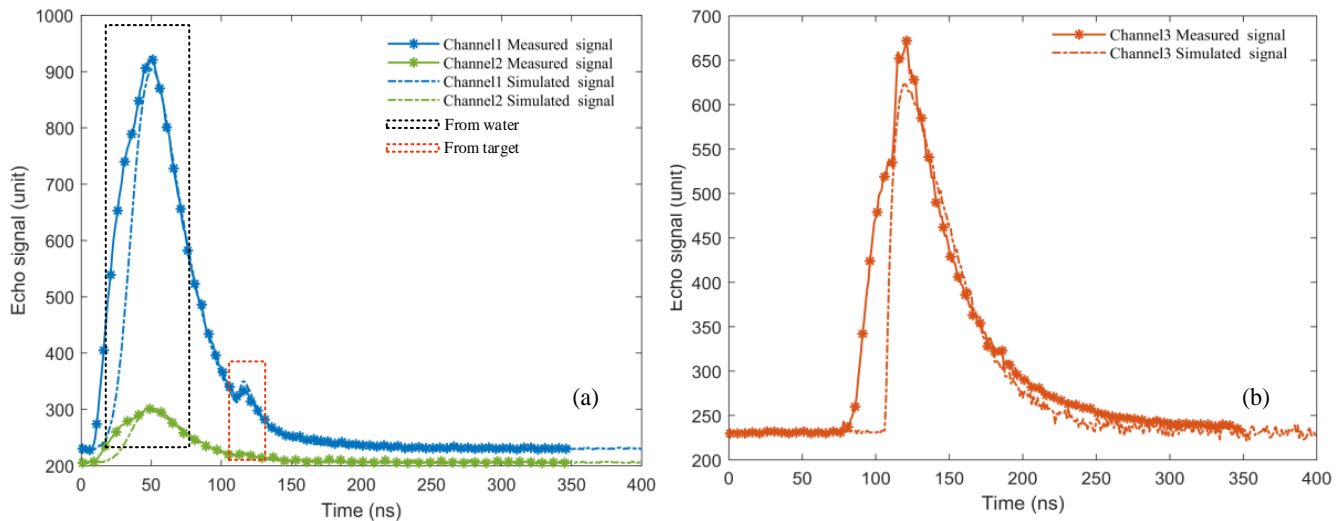


Figure 8. Signals calculated by the MULS method and measured by the Lidar in turbid water environment. (a) Near-field non-gated channels. (b) Far-field gated channel.

The far-field channel employed a PMT detector with gating function to suppress the water backscattering and enhance the signal-to-noise ratio of target echoes. The gate delay time and response time of the gating signal were set to 100 ns and 400 ns, respectively, during the measurements. Figure 8b illustrates the contrast between the calculated waveform and the measured signal of the far-field channel. It is observed that the measured signal displays a higher intensity than the simulated waveform around 100 ns, which can be attributed to signal jitter caused by factors, such as electronic noise, imperfect signal amplification, or other system-related aspects within the Lidar setup. Nonetheless, the simulated waveform generally aligns well with the measured signal, indicating the effectiveness of the range-gated mechanism in suppressing the volume backscattering signal peak. Consequently the proposed simulation method can simulate the signal of the range-gated channel properly.

The coefficient of determination (R^2) is used to verify the accuracy of the simulation method statistically [31]. The comparison of the simulated signal with field test signals for channel 1, channel 2, and channel 3 resulted in R^2 values of 0.9603, 0.9611, and 0.9479, respectively. The average R^2 value for these three channels is 0.9564. These high R^2 values demonstrate the potential of the MULS method in the signal simulation of underwater Lidar systems that utilize multiple detection channels.

4.3. Swimming Pool Verification Experiment

For validation through clear water environment, the swimming pool verification experiment was conducted on 23 December 2022. The water in the swimming pool had low levels of scattering particles and the water conditions during the experimental measurements were similar to Case I water [46], with an attenuation coefficient (c) of 0.056 m^{-1} and an absorption coefficient (a) of 0.05 m^{-1} at 532 nm. The prototype and the target were both submerged in the water and positioned on both side of the pool, as shown in Figure 9. The target was a black-painted rectangular aluminum panel with a reflectivity of 0.1, and measurements were obtained at nine different distances ranging from 3 m to 19 m at 2 m intervals, with one thousand measurements recorded at each position. To ensure precise alignment of the laser spot with the target panel, the Lidar was not scanned

during the measurements. Figure 10 displays the experimental results of targets with nine various distances.

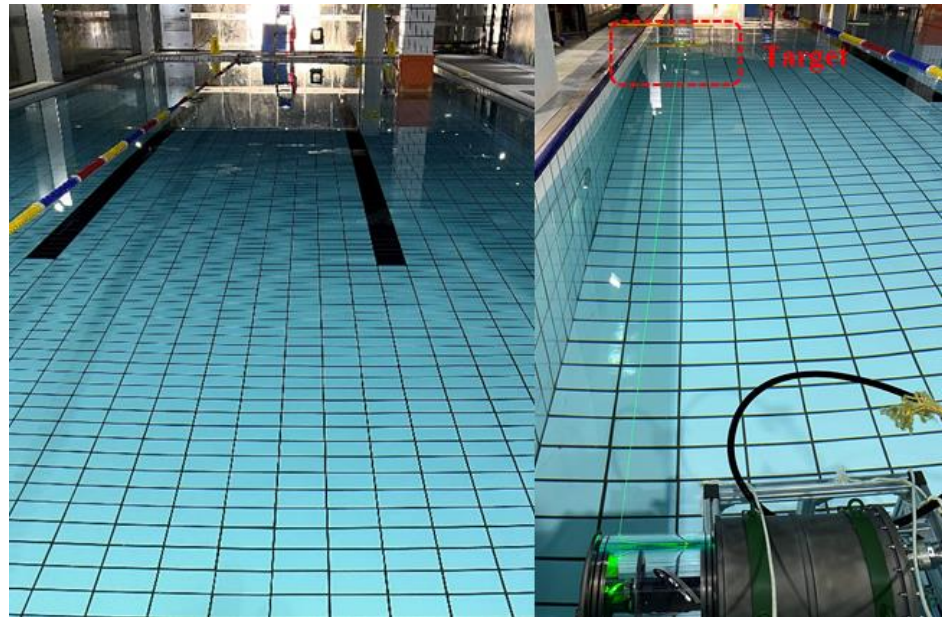


Figure 9. Verification experiments under swimming pool environment.

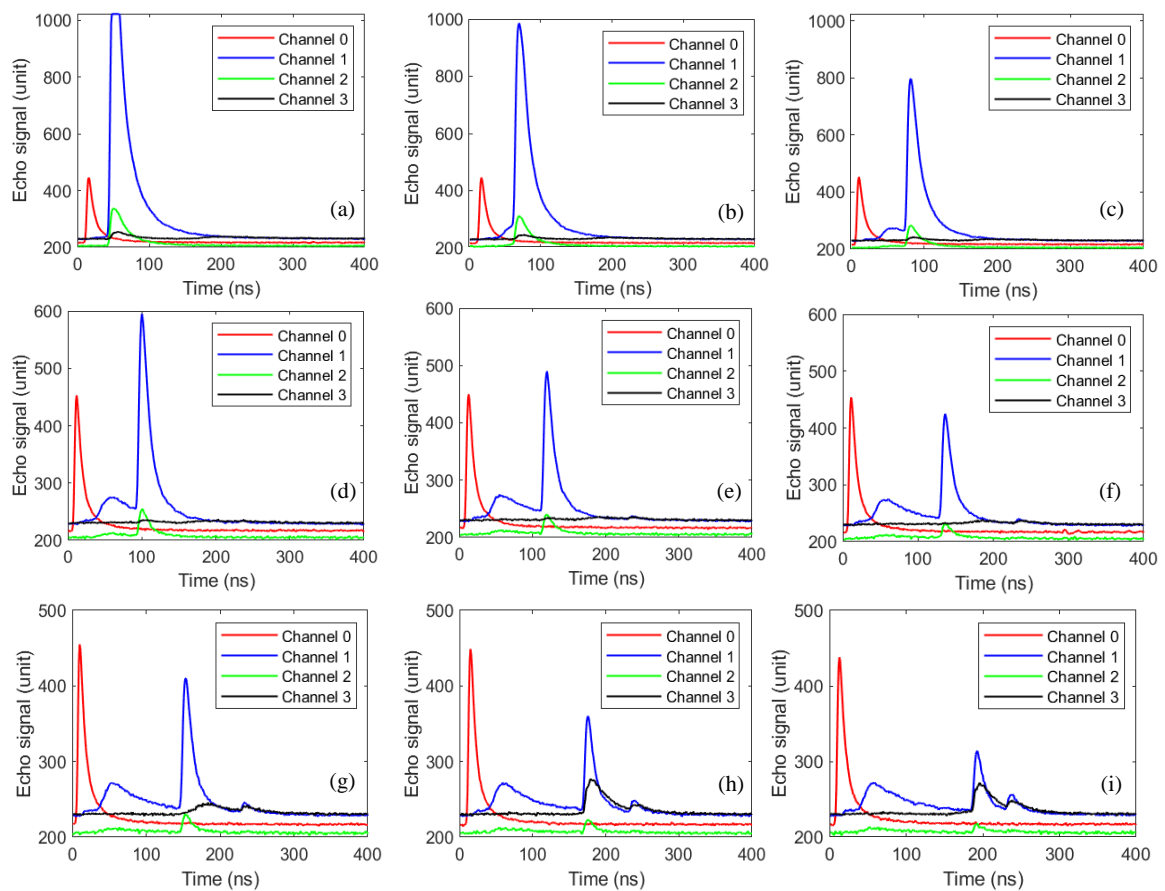


Figure 10. The measured multi-channel signals for target with different distances. (a) 3 m. (b) 5 m. (c) 7 m. (d) 9 m. (e) 11 m. (f) 13 m. (g) 15 m. (h) 17 m. (i) 19 m.

As demonstrated in Figure 10a–i, the signal level in the near-field high-gain channel 1 is greater than that in the near-field low-gain channel 2, as a result of the signal splitting mechanism. In the case of measuring a target at a distance of 3 m, the reflected signal from the target is strong, resulting in partial saturation in the target echo in high-gain channel 1, as shown in Figure 10a. Yet, the low-gain channel 2 preserves the complete waveform shape of the target echo. As the test distance increases, the intensity of the target peak in channel 2 becomes less noticeable, while the target echo peak in channel 1 remains significant. Therefore, the employment of both high- and low-gain channels can broaden the dynamic range of near-field detection and also permit more precise distance measurement.

Channel 3 is equipped with a receiver that has a gating function. This allows the detector to receive just the laser pulses reflected from the target, thereby eliminating the near-field backscatter that can overpower the sensor. The gating signal must be switched on to enable signal detection in this channel. Furthermore, by altering the delay time between the emitted laser pulse and the gate signal, the effective detection zone can be modified depending on the field test conditions. In this experiment, the gate delay time and response time of the gating signal were specifically set to 150 ns and 400 ns, respectively. Consequently, channel 3 only receive signals from the far-field but not from the water column or the near-field target. For example, the target echo begins to be recognized when the target is at a distance greater than 17 m, accompanied by the appearance of two distinctive peaks in the signals of channels 3, as indicated in Figure 10h,i. It is crucial to note that only the first peak corresponds to the target-returned echo, while the subsequent peak is a result of multi-path reflections caused by the swimming pool walls.

The measured distance data were obtained by extracting the target peak using the same methods employed in the anechoic pond verification experiment discussed in Section 4.2. Figure 11 presents the range precision and mean deviation of detection channels 1–3 at varying target positions. For each channel, range accuracy decreases as the distance of the targets increases yet remain better than 0.10 m. Notably, selecting the data of the detection channel with the highest range accuracy, specifically CH1, can lead to even more precise range measurement, with a range accuracy better than 0.06 m. Figure 11b reveals deviations between the measured distances and the actual distances, which are amplified with an increase in distance due to the pulse width of the laser and potential errors in the data processing. This bias may be mitigated through the utilization of advanced waveform processing algorithms and range correction algorithms.

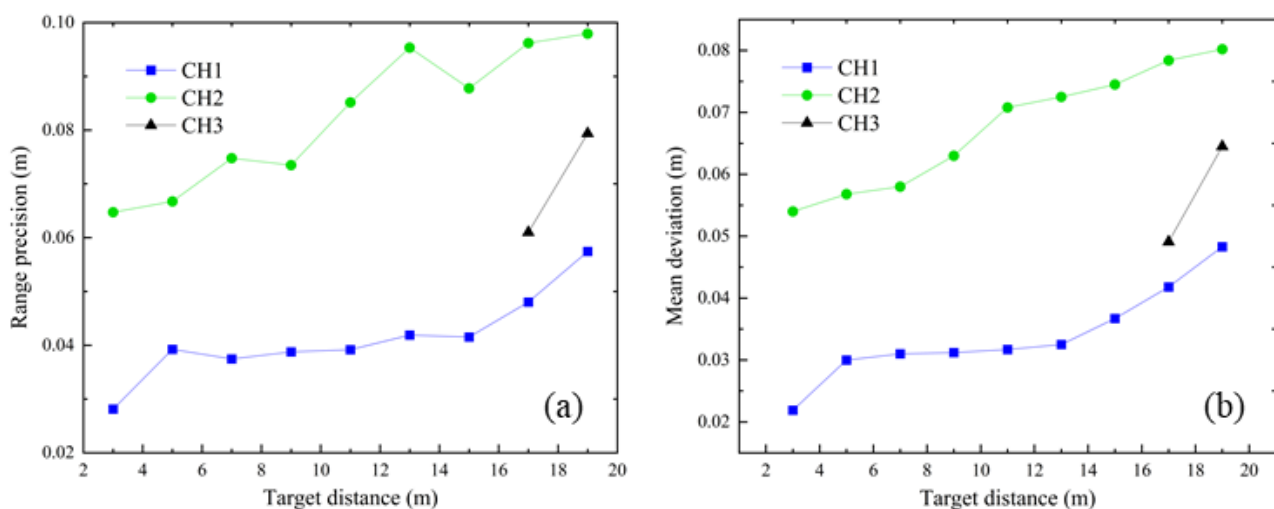


Figure 11. Range accuracy of each channel of underwater targets at different distances. (a) Range precision. (b) Mean deviation.

To validate the reliability of the proposed MULS approach in clear water environments, the simulated three-channel waveforms were compared with the swimming pool experimental results. The comparison results are shown in Figure 12. The coefficient of determination (R^2) for channel 1, channel 2, and channel 3 are 0.9663, 0.9620, and 0.9646, respectively. The average R^2 value for these three channels is 0.9643. The simulation matches well with field-tested data, which confirms the validity of the MULS approach in diverse type of water.

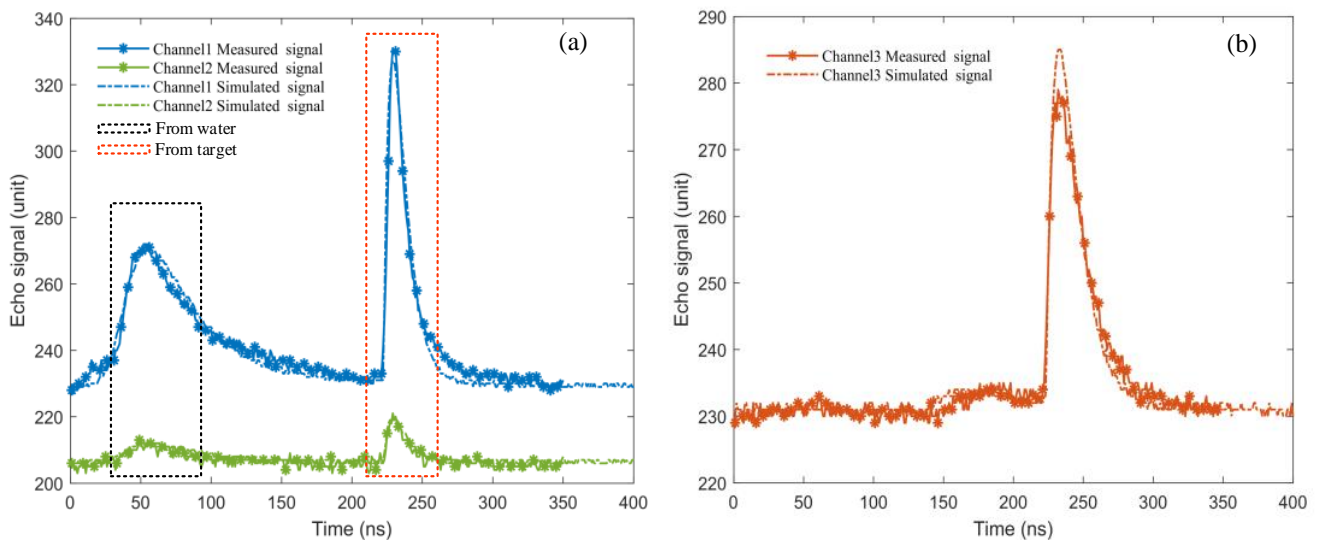


Figure 12. Signals calculated by the MULS method and measured by the Lidar in clear water environment. (a) Near-field non-gated channels. (b) Far-field gated channel.

5. Discussion

The results of both experiments and simulations demonstrate that integrating a novel paraxial multi-channel detection strategy into a Lidar prototype can greatly expand its dynamic range in underwater environments. The simulation findings are in good agreement with the experimental data, therefore proving the efficacy of the MULS method for simulating underwater Lidar systems under varying turbidity levels. Notably, various research studies have modeled the performance of oceanic Lidar systems. Among them, Abdallah [24] et al. developed a Wa-LiD simulator to simulate the Lidar waveforms from water across visible wavelength. Nevertheless, this model did not explicitly model the Lidar geometric factor, and the overlap factor was regarded as a fixed value. This premise was based on the fact that the laser footprint will always be within the FOV of the Lidar system operated from airborne platforms. In the case of underwater Lidar, where the laser beam footprint is substantially smaller as a consequence of reduced return range, it becomes crucial to explicitly characterize the Lidar geometric factor. Additionally, the detection of channel parameters, such as the resolution of digitizers, beam splitting ratio, and quantization noise, were not considered in this model. These characteristics were taken into consideration in our simulation method, which allows for a deeper understanding of the echo signals in a non-coaxial Lidar system with multiple detection channels.

In this section, we will further discuss the effects of transceiver configuration on the signal strength and evaluate the maximum detectable range of the near-field channel and the far-field channel under various water conditions based on the MULS method considering the designed Lidar prototype parameters. Moreover, the improvement in detection range gained using the multi-channel detection strategy will be discussed as well.

The overlap factor, as explained in Section 2.2.1, is a crucial factor that determines the signal strength of returning Lidar echo. To study the influence of transceiver geometric configuration on return signals under different turbidities, return signals with coaxial and non-coaxial structure under different turbidities were simulated using the identical system

parameters from Table 1, as shown in Figure 13. The power of the light scattered back from suspended particles to the Lidar system is affected by the overlap factor and water attenuation. In the near field, the geometric overlap factor has a more significant impact on the backscattering signal intensity, resulting in an increase in the signal. As the distance increases, the backscattering signal is primarily influenced by the attenuation of water, and the signal level decays exponentially. Thus, the non-coaxial Lidar signals first increase and then exponentially decline.

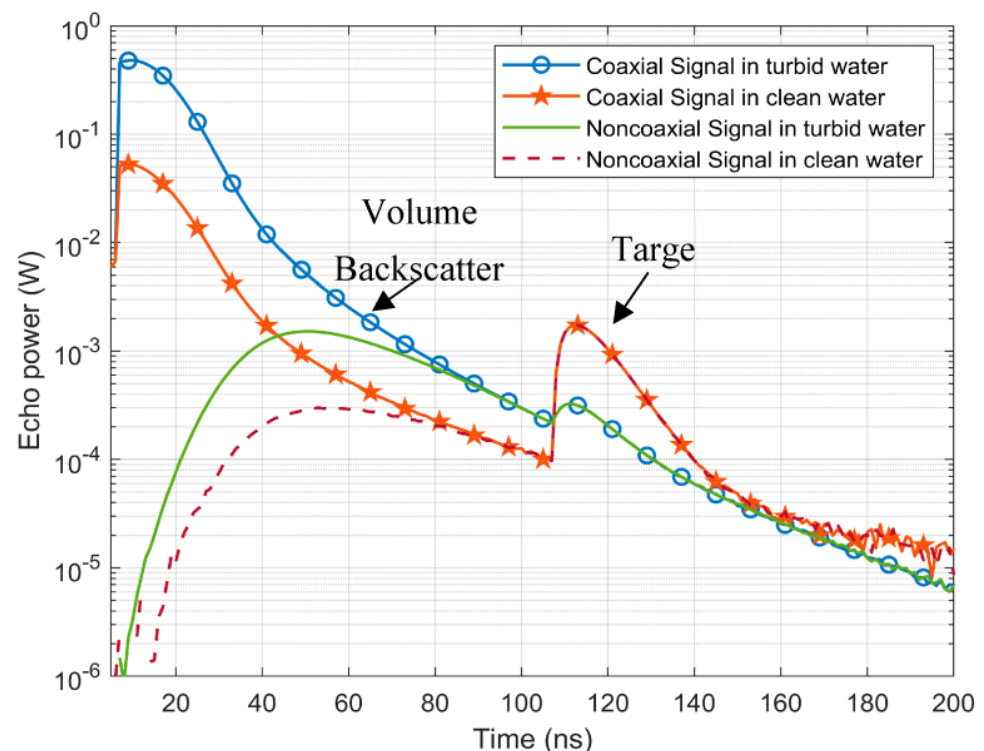


Figure 13. Comparison between the coaxial Lidar signals and the non-coaxial Lidar signals under different turbidities.

The results given in Figure 13 demonstrate that higher turbidity implies a higher peak from volume backscatter and a very low target peak [47] and the non-coaxial structure can reduce the backscattering signal level by more than two orders of magnitude in comparison to the coaxial system. However, it should be noted that the non-coaxial Lidar system introduces a detection blind area due to the spatial separation between the laser beam spot and the receiving field of the detector in the near field. As a consequence, the non-coaxial system generally has a larger minimum detection distance compared to the coaxial system.

The dynamic range of the digitizers is a critical parameter in the Lidar receiver system [17], as it permits a wide detecting range. In this study, high-speed digitizers with 10 bits were utilized in the Lidar prototype, which enable a dynamic range of 10^3 . We implemented a beam splitter to separate the signal into two channels: the far-field channel, which receives 98% of the echo signal energy, and the near-field channel, which captures the remaining 2% of the echo signal. Moreover, the output electrical signal of the near-field channel detector is further divided into high- and low-gain channels in a 9:1 ratio, thus extending the dynamic range of near-field channel to 10^4 .

To access the maximum detectable range of underwater targets with a reflectance of 0.1 using different detecting channels, we simulate the normalized Lidar signal of various channels for three distinct types of marine conditions [40]. These simulations were performed using the same systematic parameters as those presented in Table 1. The simulation results in Figure 14 show that the slope of signal attenuation is related to the optical properties of the seawater, with faster signal attenuation in more turbid water.

In this work, the far-field channel signal is detected by a range-gated detector, and the gate-open time can be adjusted by the user when they observe the signal from the near-field becomes undetectable.

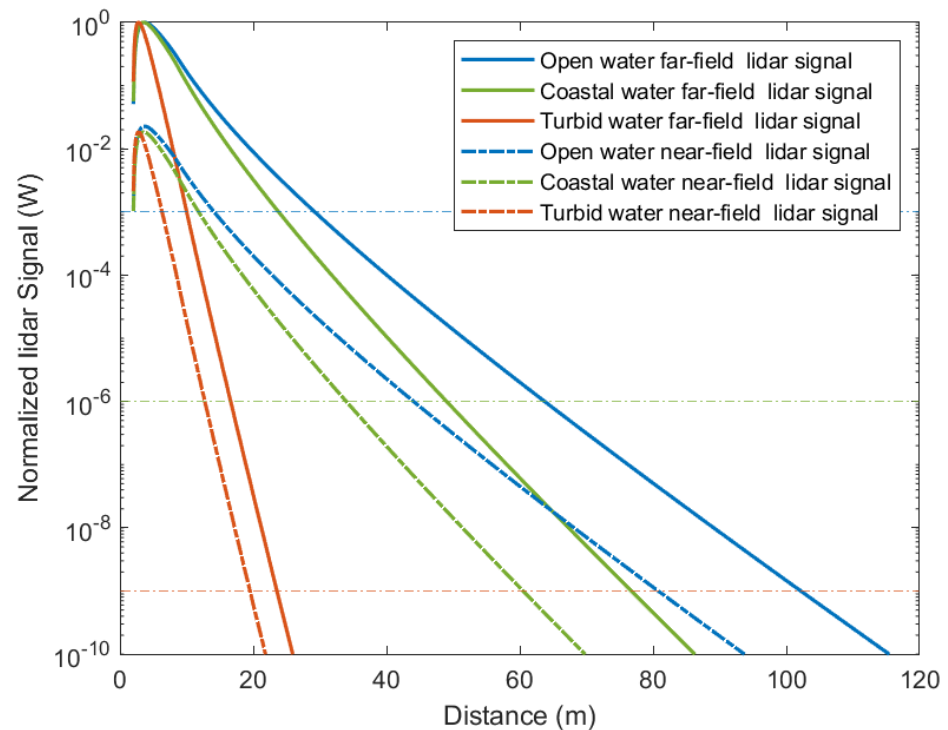


Figure 14. The normalized far-field and near-field Lidar signal under different water conditions.

Table 3 presents the maximum detectable range utilizing both multi-channel detection and single-channel strategies, along with a comparison of these two methods. As can be observed from the table, the maximum detectable range of the Lidar prototype is greatly improved by applying the proposed multi-channel detection approach compared to the single-channel detecting strategy. The improvement in maximum detectable range achieved by the multi-channel detection approach are 3.4 times, 2.5 times, and 2.3 times in clean ocean, coastal ocean, and turbid harbor water, respectively. Under clean ocean conditions, the maximum detectable range increases from 30 m to 102 m. In coastal ocean circumstances, the maximum detectable range of the far-field improves from 24 m to 60 m, while in turbid harbor, the maximum detectable range increases from 10 m to 23 m. These results demonstrate the effectiveness of the multi-channel detection approach in improving the Lidar prototype's detectable range under diverse water conditions.

Table 3. The estimated maximum detectable range based on the MULS method.

Seawater Type	Single-Channel Method (m)	Multiple Channels Strategy			Improvement (Times)
		Near-Field (m)	Far-Field (m)	Total (m)	
Clean ocean	30	44	44–102	102	3.4
Coastal ocean	24	34	34–76	60	2.5
Turbid harbor	10	12	12–23	23	2.3

6. Conclusions

In this study, we have presented the simulation and design of an underwater Lidar system that integrates a novel paraxial multi-channel detection strategy to expand the dynamic range in underwater environments. The proposed MULS approach incorporates crucial factors, such as the Lidar overlap factor, multi-channel detection settings, and data acquisition noise, which have not been adequately addressed in previous methods. This method provides a comprehensive analysis of system performance in various underwater scenarios. Verification experiments were conducted under varied water conditions to validate the simulation results and assess the system's performance. The measurements conducted using the prototype showed that the range accuracy of each channel was better than 0.11 m, and the paraxial multi-channel detection strategy effectively broadened the dynamic range and suppressed backscattering. Meanwhile, we compared the simulation results with the signals obtained from field tests conducted in both turbid and clear water environments. The correlation analysis demonstrated strong relationships between the simulated and field test signals, with correlation coefficients (R^2) of 0.9564 and 0.9643, respectively. These findings confirmed the reliability of our simulation procedure. Additionally, the simulated and theoretical analysis of our paraxial multi-channel detection design demonstrated more than two times enhancement in the maximal detectable range compared to the single-channel design.

In conclusion, our study contributes to the field of underwater Lidar systems by presenting a novel paraxial multi-channel detection strategy and providing a comprehensive simulation method for its evaluation. The validation experiments conducted under varied water conditions further strengthen the reliability of our simulation results. We believe that our findings may prove beneficial in the design and optimization of underwater Lidar systems for diverse applications, including deep-sea laser detection.

Author Contributions: All authors made significant contributions to the work. Conceptualization, W.C. and Y.H. (Yan He); funding acquisition, W.C. and S.H.; methodology, Y.C., W.C. and Y.H. (Yan He); software, Y.C., Y.H. (Yifan Huang) and S.G.; validation, Y.C., S.G., Y.L., S.H., C.H. and S.S.; writing—original draft preparation, Y.C.; writing—review and editing, Y.H. (Yan He). All authors have read and agreed to the published version of the manuscript.

Funding: This research was funded by the National Natural Science Foundation of China (61991450; 61991453) and the Shanghai “Science and Technology Innovation Action Plan” Social Development Science and Technology Project (No. 20DZ1206502).

Data Availability Statement: The data presented in this study are available upon request from the corresponding author.

Acknowledgments: We thank the anonymous reviewers for their suggestions, which significantly improved the presentation of the paper.

Conflicts of Interest: The authors declare no conflict of interest.

References

1. Sun, K.; Cui, W.C.; Chen, C. Review of Underwater Sensing Technologies and Applications. *Sensors* **2021**, *21*, 7849. [[CrossRef](#)]
2. Shen, Y.; Zhao, C.A.J.; Liu, Y.; Wang, S.; Huang, F. Underwater Optical Imaging: Key Technologies and Applications Review. *IEEE Access* **2021**, *9*, 85500–85514. [[CrossRef](#)]
3. Liu, F.H.; He, Y.; Chen, W.B.; Luo, Y.; Yu, J.Y.; Chen, Y.Q.; Jiao, C.M.; Liu, M.Z. Simulation and Design of Circular Scanning Airborne Geiger Mode Lidar for High-Resolution Topographic Mapping. *Sensors* **2022**, *22*, 3656. [[CrossRef](#)]
4. Guo, K.; Li, Q.Q.; Wang, C.S.; Mao, Q.Z.; Liu, Y.X.; Zhu, J.S.; Wu, A.L. Development of a single-wavelength airborne bathymetric LiDAR: System design and data processing. *ISPRS J. Photogramm.* **2022**, *185*, 62–84. [[CrossRef](#)]
5. Zhu, Y.D.; Liu, J.Q.; Chen, X.; Zhu, X.P.; Bi, D.C.; Chen, W.B. Sensitivity analysis and correction algorithms for atmospheric CO₂ measurements with 1.57- μ m airborne double-pulse IPDA LIDAR. *Opt. Express* **2019**, *27*, 32679–32699. [[CrossRef](#)]
6. Wulder, M.A.; Bater, C.W.; Coops, N.C.; Hilker, T.; White, J.C. The role of LiDAR in sustainable forest management. *For. Chron.* **2008**, *84*, 807–826. [[CrossRef](#)]
7. Filisetti, A.; Marouchos, A.; Martini, A.; Martin, T.; Collings, S. Developments and applications of underwater LiDAR systems in support of marine science. In Proceedings of the Oceans 2018 Mts/IEEE Charleston, Charleston, SC, USA, 22–25 October 2018.

8. Zhou, G.; Zhou, X.; Li, W.; Zhao, D.; Song, B.; Xu, C.; Zhang, H.; Liu, Z.; Xu, J.; Lin, G.; et al. Development of a Lightweight Single-Band Bathymetric LiDAR. *Remote Sens.* **2022**, *14*, 5880. [[CrossRef](#)]
9. Wang, D.D.; Xing, S.; He, Y.; Yu, J.Y.; Xu, Q.; Li, P.C. Evaluation of a New Lightweight UAV-Borne Topo-Bathymetric LiDAR for Shallow Water Bathymetry and Object Detection. *Sensors* **2022**, *22*, 1379. [[CrossRef](#)]
10. Shimada, S.; Takeyama, Y.; Kogaki, T.; Ohsawa, T.; Nakamura, S. Investigation of the Fetch Effect Using Onshore and Offshore Vertical LiDAR Devices. *Remote Sens.* **2018**, *10*, 1408. [[CrossRef](#)]
11. Collings, S.; Martin, T.J.; Hernandez, E.; Edwards, S.; Filisetti, A.; Catt, G.; Marouchos, A.; Boyd, M.; Embry, C. Findings from a Combined Subsea LiDAR and Multibeam Survey at Kingston Reef, Western Australia. *Remote Sens.* **2020**, *12*, 2443. [[CrossRef](#)]
12. Tulldahl, H.M.; Pettersson, M. Lidar for shallow underwater target detection. *Proc. Spie* **2007**, *6739*, 673906. [[CrossRef](#)]
13. McLeod, D.; Jacobson, J.; Hardy, M.; Embry, C. Autonomous Inspection using an Underwater 3D LiDAR. In Proceedings of the 2013 OCEANS, San Diego, CA, USA, 23–27 September 2013.
14. Liu, Q.; Liu, D.; Zhu, X.L.; Zhou, Y.D.; Le, C.F.; Mao, Z.H.; Bai, J.; Bi, D.C.; Chen, P.; Chen, W.B.; et al. Optimum wavelength of spaceborne oceanic lidar in penetration depth. *J. Quant. Spectrosc.* **2020**, *256*, 107310. [[CrossRef](#)]
15. Maccarone, A.; McCarthy, A.; Ren, X.M.; Warburton, R.E.; Wallace, A.M.; Moffat, J.; Petillot, Y.; Buller, G.S. Underwater depth imaging using time-correlated single-photon counting. *Opt. Express* **2015**, *23*, 33911–33926. [[CrossRef](#)]
16. Guo, S.C.; He, Y.; Chen, Y.Q.; Chen, W.B.; Chen, Q.; Huang, Y.F. Monte Carlo Simulation with Experimental Research about Underwater Transmission and Imaging of Laser. *Appl. Sci.* **2022**, *12*, 8959. [[CrossRef](#)]
17. Churnside, J.H. Review of profiling oceanographic lidar. *Opt. Eng.* **2013**, *53*, 051405. [[CrossRef](#)]
18. Churnside, J.H.; Wilson, J.J. Airborne lidar for fisheries applications. *Opt. Eng.* **2001**, *40*, 406–414. [[CrossRef](#)]
19. Kokhanenko, G.P.; Penner, I.E.; Shamanaev, V.S. Expanding the dynamic range of a lidar receiver by the method of dynode-signal collection. *Appl. Opt.* **2002**, *41*, 5073–5077. [[CrossRef](#)]
20. Imaki, M.; Ochimizu, H.; Tsuji, H.; Kameyama, S.; Saito, T.; Ishibashi, S.; Yoshida, H. Underwater three-dimensional imaging laser sensor with 120-deg wide-scanning angle using the combination of a dome lens and coaxial optics. *Opt. Eng.* **2017**, *56*, 031212. [[CrossRef](#)]
21. Sweet, M.H. A Logarithmic Photo-Multiplier Tube Photo-Meter. *J. Opt. Soc. Am.* **1947**, *37*, 432–433. [[CrossRef](#)]
22. Churnside, J.H.; Wilson, J.J.; Tatarskii, V.V. Lidar profiles of fish schools. *Appl. Opt.* **1997**, *36*, 6011–6020. [[CrossRef](#)]
23. Ooi, J.B.H.; Wong, C.J.; Loh, W.M.E.; Teo, C.K. Numerical Assessment of Horizontal Scanning LIDAR Performance Via Comparative Study Method. *Opt. Laser Eng.* **2023**, *160*, 107267. [[CrossRef](#)]
24. Abdallah, H.; Baghdadi, N.; Bailly, J.S.; Pastol, Y.; Fabre, F. Wa-LiD: A New LiDAR Simulator for Waters. *IEEE Geosci. Remote Sens. Lett.* **2012**, *9*, 744–748. [[CrossRef](#)]
25. Chen, P.; Jamet, C.; Mao, Z.H.; Pan, D.L. OLE: A Novel Oceanic Lidar Emulator. *IEEE Trans. Geosci. Remote* **2021**, *59*, 9730–9744. [[CrossRef](#)]
26. Kim, M.; Kopilevich, Y.; Feygels, V.; Park, J.Y.; Wozencraft, J. Modeling of Airborne Bathymetric Lidar Waveforms. *J. Coast. Res.* **2016**, *76*, 18–30. [[CrossRef](#)]
27. Liu, D.; Xu, P.T.; Zhou, Y.D.; Chen, W.B.; Han, B.; Zhu, X.L.; He, Y.; Mao, Z.H.; Le, C.F.; Chen, P.; et al. Lidar Remote Sensing of Seawater Optical Properties: Experiment and Monte Carlo Simulation. *IEEE Trans. Geosci. Remote Sens.* **2019**, *57*, 9489–9498. [[CrossRef](#)]
28. Liu, Q.; Cui, X.Y.; Jamet, C.; Zhu, X.L.; Mao, Z.H.; Chen, P.; Bai, J.; Liu, D. A Semianalytic Monte Carlo Simulator for Spaceborne Oceanic Lidar: Framework and Preliminary Results. *Remote Sens.* **2020**, *12*, 2820. [[CrossRef](#)]
29. Zhang, Z.H.; Chen, P.; Mao, Z.H. SOLS: An Open-Source Spaceborne Oceanic Lidar Simulator. *Remote Sens.* **2022**, *14*, 1849. [[CrossRef](#)]
30. Zhou, G.Q.; Li, C.Y.; Zhang, D.J.; Liu, D.Q.; Zhou, X.; Zhan, J. Overview of Underwater Transmission Characteristics of Oceanic LiDAR. *IEEE J. Sel. Top. Appl. Earth Obs. Remote Sens.* **2021**, *14*, 8144–8159. [[CrossRef](#)]
31. Zhou, Y.D.; Chen, W.B.; Cui, X.Y.; Malinka, A.; Liu, Q.; Han, B.; Wang, X.J.; Zhuo, W.Q.; Che, H.C.; Song, Q.J.; et al. Validation of the Analytical Model of Oceanic Lidar Returns: Comparisons with Monte Carlo Simulations and Experimental Results. *Remote Sens.* **2019**, *11*, 1870. [[CrossRef](#)]
32. Abdallah, H.; Bailly, J.S.; Baghdadi, N.N.; Saint-Geours, N.; Fabre, F. Potential of Space-Borne LiDAR Sensors for Global Bathymetry in Coastal and Inland Waters. *IEEE J. Sel. Top. Appl. Earth Obs. Remote Sens.* **2013**, *6*, 202–216. [[CrossRef](#)]
33. Chen, G.; Tang, J.; Zhao, C.; Wu, S.; Yu, F.; Ma, C.; Xu, Y.; Chen, W.; Zhang, Y.; Liu, J.; et al. Concept Design of the “Guanlan” Science Mission: China’s Novel Contribution to Space Oceanography. *Front. Mar. Sci.* **2019**, *6*, 194. [[CrossRef](#)]
34. Shen, X.; Liu, Z.P.; Zhou, Y.D.; Liu, Q.; Xu, P.T.; Mao, Z.H.; Liu, C.; Tang, L.H.; Ying, N.; Hu, M.; et al. Instrument response effects on the retrieval of oceanic lidar. *Appl. Opt.* **2020**, *59*, C21–C30. [[CrossRef](#)]
35. Gronwall, C.; Steinvall, O.; Gustafsson, F.; Chevalier, T. Influence of laser radar sensor parameters on range-measurement and shape-fitting uncertainties. *Opt. Eng.* **2007**, *46*, 106201. [[CrossRef](#)]
36. Hua, K.J.; Liu, B.; Fang, L.; Wang, H.C.; Chen, Z.; Yu, Y. Detection efficiency for underwater coaxial photon-counting lidar. *Appl. Opt.* **2020**, *59*, 2797–2809. [[CrossRef](#)]
37. Zhang, W.H.; Xu, N.; Ma, Y.; Yang, B.S.; Zhang, Z.Y.; Wang, X.H.; Li, S. A maximum bathymetric depth model to simulate satellite photon-counting lidar performance. *ISPRS J. Photogramm.* **2021**, *174*, 182–197. [[CrossRef](#)]
38. Henyey, L.G.; Greenstein, J.L. Diffuse radiation in the galaxy. *Astrophys. J.* **1941**, *93*, 70–83. [[CrossRef](#)]

39. Guenther, G.; Thomas, R. System Design And Performance Factors For Airborne Laser Hydrography. In Proceedings of the Proceedings OCEANS'83, San Francisco, CA, USA, 29 August–1 September 1983; pp. 425–430.
40. Chen, Q.; Yam, J.W.; Chua, S.Y.; Guo, N.Q.; Wang, X. Characterizing the performance impacts of target surface on underwater pulse laser ranging system. *J. Quant. Spectrosc.* **2020**, *255*, 107267. [[CrossRef](#)]
41. Li, K.P.; He, Y.; Ma, J.; Jiang, Z.Y.; Hou, C.H.; Chen, W.B.; Zhu, X.L.; Chen, P.; Tang, J.W.; Wu, S.H.; et al. A Dual-Wavelength Ocean Lidar for Vertical Profiling of Oceanic Backscatter and Attenuation. *Remote Sens.* **2020**, *12*, 2844. [[CrossRef](#)]
42. Zha, B.T.; Yuan, H.L.; Tan, Y.Y. Ranging precision for underwater laser proximity pulsed laser target detection. *Opt. Commun.* **2019**, *431*, 81–87. [[CrossRef](#)]
43. Wang, X.Z.; Zhang, M.L.; Zhou, H.Y.; Ren, X.M. Performance Analysis and Design Considerations of the Shallow Underwater Optical Wireless Communication System with Solar Noises Utilizing a Photon Tracing-Based Simulation Platform. *Electronics* **2021**, *10*, 632. [[CrossRef](#)]
44. Ehret, G.; Kiemle, C.; Wirth, M.; Amediek, A.; Fix, A.; Houweling, S. Space-borne remote sensing of CO₂, CH₄, and N₂O by integrated path differential absorption lidar: A sensitivity analysis. *Appl. Phys. B Laser Opt.* **2008**, *90*, 593–608. [[CrossRef](#)]
45. Eren, F.; Pe'eri, S.; Rzhano, Y.; Ward, L. Bottom characterization by using airborne lidar bathymetry (ALB) waveform features obtained from bottom return residual analysis. *Remote Sens. Environ.* **2018**, *206*, 260–274. [[CrossRef](#)]
46. Solonenko, M.G.; Mobley, C.D. Inherent optical properties of Jerlov water types. *Appl. Opt.* **2015**, *54*, 5392–5401. [[CrossRef](#)]
47. Castillon, M.; Palomer, A.; Forest, J.; Ridao, P. State of the Art of Underwater Active Optical 3D Scanners. *Sensors* **2019**, *19*, 5161. [[CrossRef](#)]

Disclaimer/Publisher's Note: The statements, opinions and data contained in all publications are solely those of the individual author(s) and contributor(s) and not of MDPI and/or the editor(s). MDPI and/or the editor(s) disclaim responsibility for any injury to people or property resulting from any ideas, methods, instructions or products referred to in the content.